Nanoscale

Compressive Properties of Hollow BN Nanoparticles: Theoretical Modeling and Testing in a High-Resolution Transmission Electron Microscope

Journal:	*Nanoscale*
Manuscript ID	NR-ART-01-2018-000857.R1
Article Type:	Paper
Date Submitted by the Author:	18-Mar-2018

Complete List of Authors:	Faerstein, Konstantin; National University of Science and Technology "MISIS", Kvashnin, Dmitry; Emanuel Institute of Biochemical Physics, ; National University of Science and Technology "MISIS", Inorganic Nanomaterials Kovalskii, Andrey; National University of Science and Technology "MISIS", Inorganic nanomaterials Popov, Zakhar; National University of Science and Technology MISIS , Sorokin, Pavel; Technological Institute for Superhard and Novel Carbon Materials, Structual research; Nacional\'nyj issledovatel\'skij tehnologiceskij universitet MISiS, Inorganic nanomaterials laboratory Golberg, Dmitri; National Institute for Materials Science, Shtansky, Dmitry; National University of Science and Technology "MISIS",

Journal Name

ARTICLE

Compressive Properties of Hollow BN Nanoparticles: Theoretical Modeling and Testing in a High-Resolution Transmission Electron Microscope

Received 00th January 20xx,
Accepted 00th January 20xx

DOI: 10.1039/x0xx00000x

www.rsc.org/

Konstantin L. Firestein,*[a,b] Dmitry G. Kvashnin,[a] Andrey M. Kovalskii,[a] Zakhar I. Popov,[a] Pavel B. Sorokin,*[a,c] Dmitri V. Golberg,[b,d] Dmitry V. Shtansky*[a]

Due to excellent mechanical properties, nanoparticles have a great potential as reinforcing phase in composite materials, friction modifiers in liquid lubricants, catalysts and drug-delivery agents. In the present study the mechanical analysis of individual spherical hollow BN nanoparticles (BNNPs) using a combination of *in situ* compression tests inside a high-resolution transmission electron microscope (TEM) and theoretical modelling was conducted. It was found that BNNPs display a high mechanical stiffness and a large value of elastic recovery. This enables the hollow BNNPs to exhibit considerably large cyclic deformations (up to 30% of the sphere's original external diameter) and to accumulate plastic deformation of approximately 30% of the total compression strain. Theoretical simulations allowed for elucidation of BNNPs structural changes under compression at the atomic level and explained the origin of their high stiffness and large critical deformation values.

Introduction

In recent years, there has been a great interest in the synthesis and application of boron nitride (BN) nanomaterials because of their unique mechanical properties.[1–3] Both experimental and theoretical studies show extremely high values of strength and elastic modulus for BN nanotubes,[4,5] nanoribbons,[6] and two-dimensional (2D) BN nanosheets.[7–10] By contrast, the mechanical properties of another morphological type of BN structure – spherical hollow BN nanoparticles (BNNPs) – have not been investigated in detail. However, BNNPs can be widely used as catalyst supports,[11–14] nanocarriers for drug-delivery,[15,16] additives for liquid lubricants,[17–19] reinforcing phase in metal matrix composites,[20,21] and UV-shielding materials.[22]

Nanoparticles (NPs), which are used as reinforcing agents in composite materials or as friction modifiers in liquid lubricants, must withstand large compression deformations and have the ability to accumulate large plastic strains without fracture.[23–26] Enhanced mechanical properties are also important for BNNPs used as catalysts or drug-delivery agents. For example, detailed understanding of the NP behaviour under applied load can allow for utilization of BNNPs as carriers for mechanical force-triggered drug-delivery systems in which a drug is released due to ultrasonic treatment or by changing the hemodynamic shear force in the blood vessels.[27–29] Appropriate mechanical characteristics of catalyst supports are also needed to prevent fast mechanical degradation and attrition,[30,31] hereby increasing the time of catalytic activity and selectivity.

Such set of requirements can be fulfilled by only a limited number of the material compositions. Nanostructured materials can offer very high strength, but typically they suffer from low strains to failure. Nevertheless, recently, it has been shown for CdS [32], $B_xN_yC_z$ [33] and WS_2 [34,35] compounds that a spherical shell geometry is capable of withstanding extreme stresses. *In situ* compression of nanospheres in a transmission electron microscope (TEM) revealed that these structures could sustain more than 20-50% compressive strains. [33,36] Taking into account that amorphous-like carbon nanospheres, doped with B and N, display remarkable mechanical characteristics,[33] it is assumed that crystalline BN nanoparticles can also possess both large compression strains to failure, as well as document extremely high shear stresses.

In the present study the mechanical analysis of individual BNNPs using a combination of direct *in situ* compression tests inside a high-resolution TEM (HRTEM) and theoretical modeling was conducted. Mechanical characteristics of synthesized hollow spherical BNNPs with an average size of 100-200 nm were detailed under *in situ* TEM compression. It was found that synthesized materials had displayed high mechanical stiffness and a large value of elastic recovery. This enables the hollow BNNPs to exhibit considerably large cyclic

[a] National University of Science and Technology "MISIS", Leninsky prospect 4, Moscow 119049, Russian Federation
[b] School of Chemistry, Physics and Mechanical Engineering, Queensland University of Technology (QUT), 2nd George st., Brisbane, QLD 4000, Australia
[c] Technological Institute for Superhard and Novel Carbon Materials, Troitsk, Moscow, 108840, Russian Federation
[d] International Center for Materials Nanoarchitectonics (MANA), National Institute for Materials Science (NIMS), Namiki 1-1, Tsukuba, Ibaraki 3050044, Japan
E-mail: kosty@firestein.ru, pbsorokin@misis.ru, shtansky@shs.misis.ru

deformation (up to 30% of the sphere's original external diameter) and to accumulate plastic deformation of approximately 30% of the total compression strain. Theoretical simulations allowed for elucidation of BNNPs structural changes under compression at the atomic level and explained the origin of their high stiffness and large critical deformation values.

Experimental

Synthesis of BN Nanoparticles

BNNPs were synthesized using a boron oxide-assisted chemical vapour deposition (BOCVD) in a vertical induction heating reactor, as described elsewhere.[37] As the precursor, a powder mixture of amorphous B (99.9%), MgO (analytical grade), and pure FeO, taken at a molar ratio of 3.5:0.1:1, was used. Magnesia was calcined in air at 450 °C for 1 h for dehydration before weighing. The precursor mixture was mechanically ground in a mechanical alumina mortar for 1 h with an addition of isopropanol. Argon of 99.993% purity was used as a carrying gas. It was supplied from the bottom of the reactor, and ammonia of 99.98% purity was used as the reactant gas, the latter was supplied from the top of the reactor. The furnace chamber was first evacuated to 10^{-2} mbar under slow heating to 360 ºC. Then, argon was fed at a rate of 500 cm^3/min and, upon reaching the total pressure of 1 bar, heating to the synthesis temperature was started. When the synthesis temperature was reached, ammonia was supplied at a feeding rate of 100 cm^3/min. Syntheses were carried out under the temperature gradient along the reactor height with a higher temperature (1310 ºC) in the precursor zone and a lower temperature (700-750 °C) in the BN particles outlet zone. The temperature of the powder mixture was controlled by an optical pyrometer during the whole process.

Structural Characterization

The microstructure of as-synthesized BNNPs was studied using a JEM7600F scanning electron microscope (JEOL) and a JEM-2100 transmission electron microscope (JEOL) equipped with an energy-dispersive spectrometer (Oxford Instruments).

In situ Compression Tests on BNNPs

In situ TEM compression tests on individual BNNPs were performed in a JEM 2100 microscope (JEOL) using a depth-sensing PI 95 TEM Picoindenter (Hysitron). The BNNP deformation was video-recorded in real time using "Radius" and "Hysitron TriboScan" software applications (Olympus and Hysitron, respectively). During deformation, force-time and force-displacement curves were recorded. The compression tests were carried out using a diamond flat end conical tip with 1 μm diameter of the top circle. Samples were loaded and unloaded at a rate of 2.5 nm *per* second. For *in situ* TEM compression testing, BNNPs were deposited onto the wedge located on the surface of a Si substrate using BNNP suspension in isopropanol.

Theoretical Simulations

The mechanical response of BNNPs was described in the framework of the classical molecular dynamics (MD) method implemented in LAMMPS package.[38] The advantage of this method is the possibility of large system simulation at a sufficiently high calculating speed. To achieve better relaxation of the structures, the simulation of annealing at a temperature decreasing from 800 K to 100 K during 40 ps was applied, while the maximum interatomic forces became less or equal to 0.05 eV/Å. The atomic interactions between B and N atoms in BNNP were described by the Tersoff 3-body potential[39] implemented in LAMMPS. We found that the yielded values of in-plane stiffness (276 N/m) and flexural rigidity (1.21 eV) of h-BN fit well corresponding DFT data: 271 N/m and 1.29 eV,[40] respectively. It allows to propose that mechanical properties BNNP also will be predicted with high accuracy.

It is impossible to generate a perfect BN particle consisting of hexagons only (at the very least, 12 pentagons are required by Euler theorem), so our initial models were made of six grains of a perfect h-BN connected via grain boundaries. The energy preferable atomic structures of all models were obtained using simulation annealing from 800 to 100 K. After annealing the extra atoms were removed from the considered models and small corrugations of disordered hexagonal *h*-BN layers (observed experimentally as a turbostratic BN, see below) were obtained. Simulated BNNPs with various diameters (from 9 to 32 nm) contained up to 10^6 atoms.

In order to calculate mechanical characteristics, considered nanoparticles were gradually compressed under a constant loading force with a small step, of about 0.7 Å. After reaching the certain compression ratio, the load from the sphere was gradually released with the same step. From the energy-strain curves of compression process the elastic constants of each sphere were defined.

Results and Discussion

Microstructure of as-synthesized BNNPs

Low- and HRTEM images of as-synthesized BNNPs are presented in Fig. 1a-c. The BNNPs with an average size of 100-200 nm showed nearly spherical morphology with a hollow central part and the shells with a thickness in the range of 15-30 nm (Fig. 1a). The BNNP shells consisted of numerous *h*-BN subgrains, with hexagonal planes being approximately parallel to the tangent to the particle surface, separated by coherent or self-coherent grain boundaries, as indicated in Fig. 1b. Misfit dislocations were frequently observed at the subgrain boundary interfaces. Closer to the BNNP surfaces, the density of defects increased and the outer parts of the shells were formed by rather small and highly disordered regions, several nm thick (Fig. 1c). This type of structure can be described as a turbostratic BN (*t*-BN), with hexagonal or rhombohedral basal planes roughly parallel to each other but randomly rotated about the layer normal.[41]

To in detail understand the atomic geometry of the synthesized hollow particles MD simulations were performed. According to the experimental results, the BNNP models reproduce the main structural features of the synthesized particles pretty well (Fig. 1d). Simulated nanospheres have a pronounced layered structure with the same ratio between sizes of a hollow area and wall thickness (Fig. 1e). Because of the complexity of the geometric modelling of the regarded nanoparticles, proposed models initially contain six grains with the peculiar grain boundaries. After annealing, small corrugations of the hexagonal BN (*h*-BN) layers were observed.

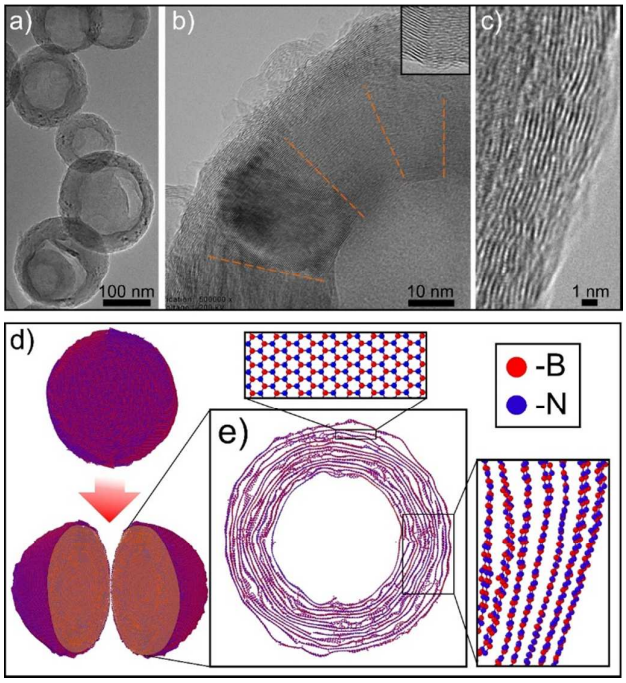

Fig. 1 (a) Low- and (b,c) high-resolution TEM images of hollow BNNPs demonstrating (b) crystalline and (c) layered (with the disordered outer part) structures; d) Theoretical model of the experimentally studied nanoparticles with (e) a magnified slice, where characteristic structural features are depicted. The colour code of atomic species is presented in the inset.

In situ TEM Compression Testing of BNNPs

The particles were tested in the process of multi-cycle compression deformation with a gradually increasing load (in order to determine the threshold of the plastic deformation). Fig. 2 shows a set of representative images captured during video-recording of the compression process on a single BNNP with the outer diameter and the shell thickness of ~175 and ~30 nm, respectively. The BNNP was subjected to seven consecutive loading-unloading cycles at a maximum load in the end of each cycle of 5.1, 5.4, 6.0, 7.7, 9.2, 12.0, and 14.5 μN (Fig. 2j). Fig. 2a presents the TEM image of BNNP before tests, whereas Fig. 2b,c demonstrates the sphere shape after three and four consecutive loading-unloading cycles, respectively. Next six TEM micrographs show three pairs of BNNP images recorded during 5, 6 and 7 loops at the maximum loads and after the load removal. At a low applied load, typically below 10 μN, the BNNP retained its size and spherical shape. Since BNNPs were rather frequently adhered to the punch surface after the load removal, the percentage of elastic recovery is difficult to determine. According to the loading-unloading curves presented in Fig. 2k, the maximum compression strain during the fifth cycle was approximately 25% of the original sphere diameter. Fig. 2d,e shows that the part of the shell, that was in contact with the indenter punch, was pushed inside the BNNP during loading, but returned to its original position after the load was removed (Fig. 2e). Since the interfaces between adjacent *h*-BN grains are roughly parallel to the direction of the applied load (Fig. 1b), it is reasonable to assume that the deformation of shell proceeds by grain boundary sliding, as shown by arrows in Fig. 2d,e. This assumption is also confirmed by discrete yielding events observed on the loading curve (Fig. 2k). It was demonstrated that atomic layers in *h*-BN nanotubes are very flexible and may fully restore their original shape after reloading.[42] The in-plane measured bending angle reached 70° or even more. Since the incline of loading and unloading curves was different (Fig. 2k), the sphere stiffness was determined from the slope of the linear part of the both curves and the values of about ~170 N/m and ~10^3 N/m were obtained. Note that each of the methods is not devoid of certain drawbacks. For instance, the BNNP can be shifted during preloading stage and/or subjected to some plastic deformation upon further loading (see Fig. 2k). During unloading, the BNNPs were occasionally observed to stick to the indenter tip, which can lead to overestimation of the stiffness values. Our results indicate that during multi-cycle loading (4 cycles), the BNNP withstands an applied load up to 9.2 μN and demonstrates a relatively high value of elastic recovery, wherein the maximum contact area is 1.15×10^4 nm^2 (as was measured directly from Fig. 2d assuming a circular contact area) and the maximum contact pressure reaches 0.8 GPa. It is interesting to look at the obtained value with respect to the contact pressure achieved during standard tribological tests. Assuming an applied load of 1-10 N and the size of tribological contact of 100 μm, the values of contact pressure in the range of 0.13-1.3 GPa are calculated. These agree well with the experimental value obtained during *in situ* TEM tests. During the sixth cycle, when the applied load was increased to 12 μN, the maximum compression strain became of ~27% of the initial particle diameter. The BNNP demonstrated a high percentage of elastic recovery and a 5% residual compression strain (Fig. 2g). Final deformation loop, with the maximal load of 14.5 μN, led to 30% and 10% maximal and residual compression strains, respectively (Fig. 2h,i). Thus the high strength enables the hollow BNNP to exhibit considerable cyclic deformation (up to 30% of the sphere's original external diameter) and to accumulate plastic deformation of approximately 30% of the total compression strain.

Theoretical analysis of BNNPs behavior under the strain

At the next step the theoretical simulation of compression process of BNNPs was carried out. In Fig. 3a the main steps of the loading process with an indication of the corresponding compression ratios are presented. The calculated strain energy at each step of the compression (Fig. 3b, black curve) allowed us to obtain mechanical characteristics of the material. The BNNP behaviour under its loading up to 55% compressive strain was studied.

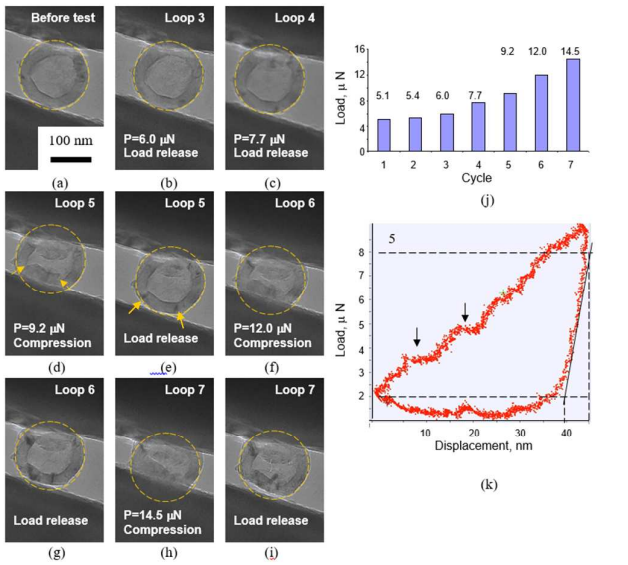

Fig. 2 Snapshots (a-i) obtained from a video recorded during consecutive *in situ* TEM compression tests on an individual BNNP under increasing load (j). Loading-unloading curves recoded during the 5th cycle (k).

It was found that compression of the BNNP had led to corrugation of the outer layers with distortion propagation within the whole nanosphere structure under the increased degree of loading (Fig. 3a). Nanoparticles behave fully elastically under a compressive strain up to 30% and even after 50% strain (followed by unloading) they were able to recover their initial shape. A higher value of critical compression strain predicted theoretically in comparison with the experimental figure (30%) can be explained by a fact that the considered model contains a small number of defects, which leads to enhanced mechanical characteristics.

At the 55% deformation the strain energy suddenly drops. This indicates the appearance of irreversible changes within the atomic structure (see the inset in blue frame in Fig. 3a), the formation of the interlayered bonds, and a partial transformation of *h*-BN to cubic phase (*c*-BN). The phase transition is also indicated by a fact that the energy curve does not return to its initial position after unloading (Fig. 3b, blue line) and displays aminimum at the 40% compression ratio (density of *c*-BN is ~40% higher than that of *h*-BN). The relaxed transformed BNNP structure with indicated sp^3 BN bonds is drawn in the inset of Fig. 3b.

For all considered BNNPs with various diameters the elastic constants were calculated from the loading curves (Fig. 3c). It was found that the diameter increase had led to the gradual stiffening of BNNPs with a monotonous tendency to reveal the elastic constants of ~300 N/m at a diameter of ~16 nm, see Fig. 3c, which is already very close to the value of h-BN in-plane stiffness. [40] The blue and red dots correspond to theoretically estimated and experimentally measured values, respectively. Theoretically obtained numbers display good agreement with the experimental data and allow us to conclude that all models of BNNPs (with a size more than 16 nm) display mechanical stiffness close to the average stiffness (170-200 N/m) determined from the loading curves of experimentally obtained nanoparticles with sizes of hundreds of nanometers. Thus, in the further computations only 16 nm sized BNNP was analyzed. It should be noted that the elastic constant defined *via* the unloading curve is in average 1.5-2 times higher. This also corresponds to the experimental data.

In Fig. 3d the summary of simulation results is presented. All considered BNNPs possess the critical compression strains and critical applied forces in the vicinity of ~40% and ~5 μN values, respectively. This also agrees well with the experimental results.

The description of the impact of structural defects onto BNNP properties was modeled under uniform inclusion of the vacancy defects into the atomic structure. Vacancies are the most common and essential type of defects in a nanostructure. In this study, the vacancy defects on both boron and nitrogen atoms were considered. In Fig. 3e the dependence of the elastic constant and the critical loading force on the defect concentration (BNNP diameter is 16 nm) is presented. The presence of defects linearly decreases the stiffness of BNNPs (from 278.85 N/m at 0% to 97.81 N/m at 6% of vacancy defects). Nevertheless, the critical fracture force only slightly decreases with increasing the defect concentration. It drops only from 3.35 to 2.85 μN for 6% of defects.

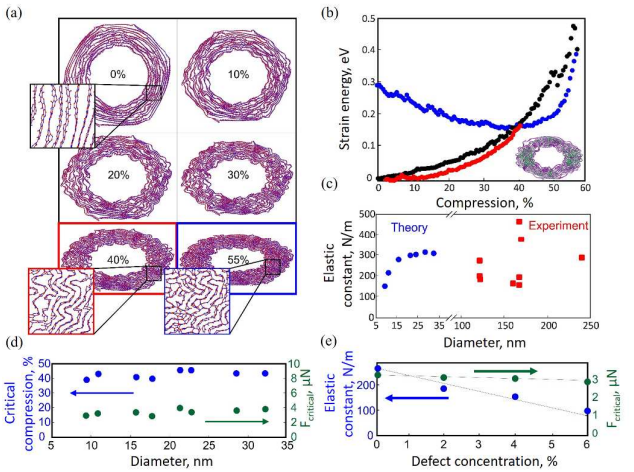

Fig. 3 a) Main snapshots of the compression process of a BNNP with a mean diameter of ~16 nm. Red and blue boxes depict atomic structure of BNNP before and after critical degree of compression after which the irreversible structural changes took place; b) Strain energy dependence for BNNP with an average diameter of ~16 nm (curves depicted in red and blue colours correspond to the unloading data before and after critical compression strain). The inset presents a relaxed structure of BNNP after

the phase transition induced by the critical strain (see text for details). The sp^3-hybridized bonds are marked in green colour, whereas sp^2-hybridized bonds are depicted in pink; (c) Dependences of the elastic constant values on the BNNP diameter (red and blue dots represent experimental and theoretical data, respectively); d) Dependences of the critical force and critical compression values on the nanoparticle size and (e) on the defect concentration; BNNP diameter is ~16 nm.

In situ TEM Compression Testing of BNNPs under the higher applied load

In order to achieve the fracture limit, BNNPs were tested in compression under the higher applied load. The tested BNNP, presented in Fig. 4a, had the outer diameter of 190 nm, and the shell thickness of 35 nm. After the first loading-unloading cycle, at a maximum load of 18.7 μN, which corresponds to the maximal compression strain of 21% of the original sphere diameter, the contact zone became flat indicating 34% of plastic deformation (Fig. 4b,c). During subsequent two cycles of deformation under loads of 19.1 μN and 20.1 μN (not shown), the BNNP largely restored its initial shape, by nearly 82-88%. During the fourth loop, the BNNP withstood an applied load of 24.4 μN without failure, whereas the maximum contact area, estimated assuming a circular contact area, became 2.5×10^4 nm^2 and the maximum contact pressure reached 1 GPa (Fig. 4d,e). The HRTEM image, taken after compression test presented in Fig. 4g, additionally illustrates that the deformation of BNNP proceeds not only by the grain boundary sliding but also through bending and kinking of *h*-BN layers, being in a good agreement with the simulation results. The sphere stiffness, determined from the slope of the linear part of the loading and unloading curves, was approximately 0.76×10^3 N/m and 4.4×10^3 N/m, respectively (Fig. 4h). These results indicate that the hollow BNNPs are able to withstand a large compressive deformation to failure (up to 50% of the sphere's original external diameter) and to accumulate plastic deformation of about 39% of the total compression. The final test under maximum load of 62.1 μN led to the destruction of the BNNP and its ultimate flattening (Fig. 4f). The loading curve changed its shape and became consisted of two parts: a mild-slope part at low loads and the steep part at high loads (Fig. 4i). The slope change indicates that the internal space becomes closed and the material starts to more effectively resist to loading. As a result, the stiffness value determined from the linear part of the unloading curve increased up to 8.5×10^3 N/m.

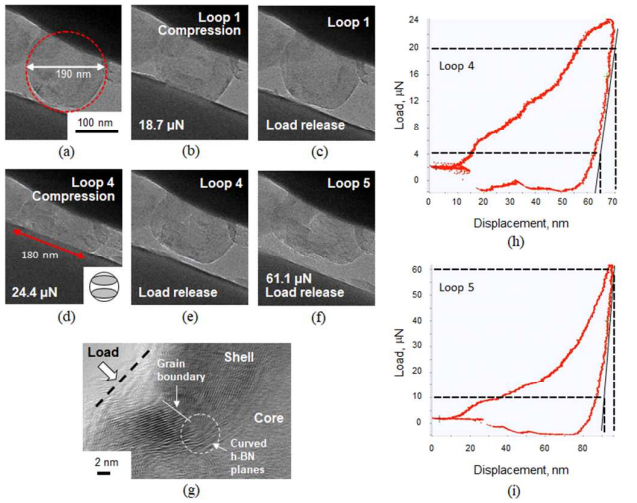

Fig. 4 Screenshots (a-f) from a video showing hollow BNNP deformation during in situ consecutive compression runs under a gradually increased load. (g) HRTEM image of a BNNP after compression test displaying the specific deformation character, i.e. bending and kinking of *h*-BN layers. (h, i) Loading-unloading curves recoded during the 4th and 5th cycles.

One possible technological application of the above-described hollow BNNPs would be their utilization as additives to liquid lubricants. Since the hollow BNNPs withstand a relatively large applied load and possess high degree of elastic recovery, their main lubrication mechanism under low pressure could be rolling. [43] At the higher loads, the contact area between BNNPs and counterpart material becomes flat with a high degree of alignments of the basal hexagonal planes parallel to the friction direction (Fig. 5). This minimizes the resistance to shear during friction. It is worth noting that hollow BNNPs may also play a role of spacers between friction surfaces, hereby preventing adhesion and sticking of a material being under tribological contact. All these factors may favourably affect lubricity of BNNPs.

Finally, note that the prediction of sp^2 to sp^3 transformation is consistent with the model of stress-induced c-BN formation. It has been well established that a high compressive stress of several GPa is needed for the growth of c-BN films. [44–46] A more detailed TEM study of the BNNP after deformation revealed that the sp^2-bonded BN is highly strained due to the formation of a large number of interlinked sp^2 layers with high interface energies (see, for instance, numerous interlinked shells marked in Fig. 5d, inset).

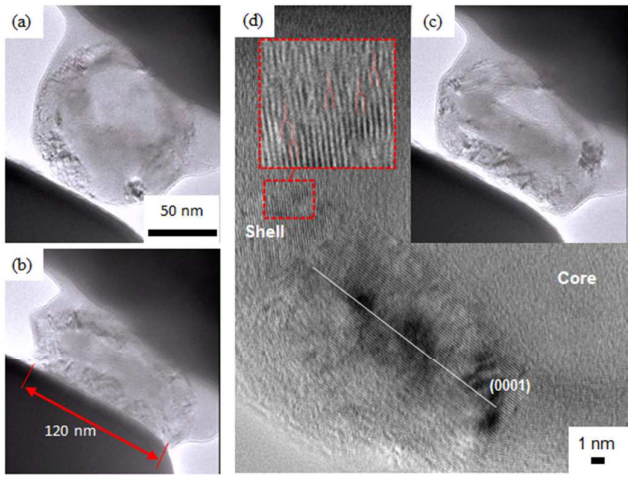

Fig. 5 TEM images of a representative BNNP obtained from a video recorded at (a) zero deformation, (b) maximal deformation, and (c) after a load release. (d) High resolution TEM image of the hollow BNNP shown in (c). The inset in (d) illustrates the appearance of numerous interlinked BN layers within the highly-compressed region.

Conclusions

By means of molecular dynamics simulations paired with direct *in situ* compression tests in a high-resolution TEM the mechanical behaviour of BNNPs of various diameters was studied in detail. It was found that the BNNPs display a high mechanical stiffness and a large value of elastic recovery. This enables them to exhibit considerably large cyclic deformation (up to 30% of the sphere's original external diameter) and to accumulate plastic deformation of approximately 30% of the total compression strain. A good agreement with the experimental data in regard of critical compression strain values (40% by the theoretical predictions and 30% by the experimental observations), critical force, and elastic constants was documented. It was found that after reaching the critical compression strain the irreversible atomic structure changes had occurred being accompanied by the formation of the interlayered bonds and partial transformation of *h*-BN to *c*-BN phase within BNNPs.

Conflicts of interest

There are no conflicts to declare

Acknowledgements

The work was supported by the Ministry of Education and Science of the Russian Federation (D.G.K. thanks Increase Competitiveness Program of NUST "MISiS" No. K2-2016-002, A.M.K. and D.V.S. are grateful to the State task No. 11.937.2017/ПЧ). P.B.S. acknowledges the financial support of the RFBR, according to the research project No. 16-32-60138 mol_a_dk. K.F. and D.G. also acknowledge the Australian Research Council (ARC) for funding in the frame of ARC Laureate Project No. FL160100089 and QUT Project No. 322120-0355/51. D.G.K. also acknowledges Grant of President of Russian Federation for government support of young PhD scientists (MK- 3326.2017.2).

Notes and references

1 J. Yin, J. Li, Y. Hang, J. Yu, G. Tai, X. Li, Z. Zhang and W. Guo, *Small*, 2016, **12**, 2942–2968.
2 Z. Zhang, Y. Liu, Y. Yang and B. I. Yakobson, *Nano Lett.*, 2016, **16**, 1398–1403.
3 A. Pakdel, Y. Bando and D. Golberg, *Chem. Soc. Rev.*, 2014, **43**, 934–959.
4 X. Wei, M. S. Wang, Y. Bando and D. Golberg, *Adv. Mater.*, 2010, **22**, 4895–4899.
5 N. G. Chopra and A. Zettl, *Solid State Commun.*, 1998, **105**, 297–300.
6 H. Zeng, C. Zhi, Z. Zhang, X. Wei, X. Wang, W. Guo, Y. Bando and D. Golberg, *Nano Lett.*, 2010, **10**, 5049–5055.
7 L. Song, L. Ci, H. Lu, P. B. Sorokin, C. Jin, J. Ni, A. G. Kvashnin, D. G. Kvashnin, J. Lou, B. I. Yakobson and P. M. Ajayan, *Nano Lett*, 2010, **10**, 3209–3215.
8 L. Boldrin, F. Scarpa, R. Chowdhury and S. Adhikari, *Nanotechnology*, 2011, **22**, 505702–505708.
9 I. Nikiforov, D.-M. Tang, X. Wei, T. Dumitrică and D. Golberg, *Phys. Rev. Lett.*, 2012, **109**, 025504.
10 A. Falin, Q. Cai, E. J. G. Santos, D. Scullion, D. Qian, R. Zhang, Z. Yang, S. Huang, K. Watanabe, T. Taniguchi, M. R. Barnett, Y. Chen, R. S. Ruoff and L. H. Li, *Nat. Commun.*, 2017, **8**, 15815–15823.
11 Y. Wang, L. Shi, W. Lu, Q. Sun, Z. Wang, C. Zhi and A. H. Lu, *ChemCatChem*, 2017, **9**, 1363–1367.
12 T. Ohashi, Y. Wang and S. Shimada, *J. Mater. Chem.*, 2010, **20**, 5129–5135.
13 K. L. Firestein, D. G. Kvashnin, A. N. Sheveyko, I. V. Sukhorukova, A. M. Kovalskii, A. T. Matveev, O. I. Lebedev, P. B. Sorokin, D. Golberg and D. V. Shtansky, *Mater. Des.*, 2016, **98**, 167–173.
14 H. Si, G. Lian, J. Wang, L. Li, Q. Wang, D. Cui and C. P. Wong, *ACS Appl. Mater. Interfaces*, 2016, **8**, 1578–1582.
15 I. V Sukhorukova, I. Y. Zhitnyak, A. M. Kovalskii, A. T. Matveev, O. I. Lebedev, X. Li, N. A. Gloushankova, D. Golberg and D. V Shtansky, *ACS Appl. Mater. Interfaces*, 2015, **7**, 17217–17225.
16 X. Li, X. Wang, J. Zhang, N. Hanagata, X. Wang, Q. Weng, A. Ito, Y. Bando and D. Golberg, *Nat. Commun.*, 2017, **8**, 13936.
17 W. Han, Z. Ma, S. Liu, C. Ge, L. Wang and X. Zhang, *Ceram. Int.*, 2017, **43**, 10192–10200.
18 M. S. Charoo and M. F. Wani, *Lubr. Sci.*, 2017, **29**, 241–254.
19 Q. Wan, Y. Jin, P. Sun and Y. Ding, in *Procedia Engineering*, 2015, vol. 102, pp. 1038–1045.
20 K. L. Firestein, A. E. Steinman, I. S. Golovin, J. Cifre, E. A. Obraztsova, A. T. Matveev, A. M. Kovalskii, O. I. Lebedev, D. V. Shtansky and D. Golberg, *Mater. Sci. Eng. A*, 2015, **642**, 104–112.
21 R. Gostariani, M. A. Asadabad, M. H. Paydar and R. Ebrahimi, *Adv. Powder Technol.*, 2017, **28**, 2232–2238.
22 Y. Fu, Y. Huang, W. Meng, Z. Wang, Y. Bando, D. Golberg, C. Tang and C. Zhi, *Nanotechnology*, 2015, **26**, 115702.
23 Y. Y. Wu, W. C. Tsui and T. C. Liu, *Wear*, 2007, **262**, 819–825.
24 V. N. Bakunin, A. Y. Suslov, G. N. Kuzmina, O. P. Parenago and A. V. Topchiev, *J. Nanoparticle Res.*, 2004, **6**, 273–284.

25 M. Yamaguchi, J. Bernhardt, K. Faerstein, D. Shtansky, Y. Bando, I. S. Golovin, H. R. Sinning and D. Golberg, *Acta Mater.*, 2013, **61**, 7604–7615.
26 R. Casati and M. Vedani, *Metals*, 2014, **4**, 65–83.
27 Y. Zhang, J. Yu, H. N. Bomba, Y. Zhu and Z. Gu, *Chem. Rev.*, 2016, 116, 12536–12563.
28 J. Di, J. Yu, Q. Wang, S. Yao, D. Suo, Y. Ye, M. Pless, Y. Zhu, Y. Jing and Z. Gu, *Nano Res.*, 2017, **10**, 1393–1402.
29 B. Kim, S. Yoo, Y. J. Kim, J. Park, B. Kang, S. Haam, S. W. Kang, K. Kang and U. Jeong, *Adv. Mater. Interfaces*, 2016, **3**, 1500803.
30 C. H. Bartholomew, *Appl. Catal. Gen.*, 2001, **212**, 17–60.
31 C. Couroyer, M. Ghadiri, P. Laval, N. Brunard and F. Kolenda, *Oil Gas Sci. Technol.*, 2000, **55**, 67–85.
32 Z. W. Shan, G. Adesso, A. Cabot, M. P. Sherburne, S. A. S. Asif, O. L. Warren, D. C. Chrzan, A. M. Minor and A. P. Alivisatos, *Nat. Mater.*, 2008, **7**, 947–952.
33 S. Ozden, C. S. Tiwary, J. Yao, G. Brunetto, S. Bhowmick, S. Asif, R. Vajtai and P. M. Ajayan, *Carbon*, 2016, **105**, 144–150.
34 C. Shahar, D. Zbaida, L. Rapoport, H. Cohen, T. Bendikov, J. Tannous, F. Dassenoy and R. Tenne, *Langmuir*, 2010, **26**, 4409–4414.
35 F. Xu, T. Kobayashi, Z. Yang, T. Sekine, H. Chang, N. Wang, Y. Xia and Y. Zhu, *ACS Nano*, 2017, **11**, 8114–8121.
36 W. Yang, S. Mao, J. Yang, T. Shang, H. Song, J. Mabon, W. Swiech, J. R. Vance, Z. Yue, S. J. Dillon, H. Xu and B. Xu, *Sci. Rep.*, 2016, **6**, 24187.
37 A. M. Kovalskii, A. T. Matveev, O. I. Lebedev, I. V. Sukhorukova, K. L. Firestein, A. E. Steinman, D. V. Shtansky and D. Golberg, *CrystEngComm*, 2016, **18**, 6689–6699.
38 S. Plimpton, *J. Comput. Phys.*, 1995, **117**, 1–19.
39 A. Kınacı, J. B. Haskins, C. Sevik and T. Çağın, *Phys. Rev. B*, 2012, **86**, 115410.
40 K. N. Kudin, G. E. Scuseria and B. I. Yakobson, *Phys Rev B*, 2001, **64**, 10.
41 D. V. Shtansky, O. Tsuda, Y. Ikuhara and T. Yoshida, *Acta Mater.*, 2000, **48**, 3745–3759.
42 D. Golberg, X. D. Bai, M. Mitome, C. C. Tang, C. Y. Zhi and Y. Bando, *Acta Mater.*, 2007, **55**, 1293–1298.
43 L. Rapoport, V. Leshchinsky, M. Lvovsky, O. Nepomnyashchy, Yu Volovik and R. Tenne, *Ind. Lubr. Tribol.*, 2002, **54**, 171–176.
44 M. Zeitler, S. Sienz and B. Rauschenbach, *J. Vac. Sci. Technol. Vac. Surf. Films*, 1999, **17**, 597–602.
45 D. R. McKenzie, W. D. McFall, W. G. Sainty, C. A. Davis and R. E. Collins, *Diam. Relat. Mater.*, 1993, **2**, 970–976.
46 D. V. Shtansky, Y. Yamada-Takamura, T. Yoshida and Y. Ikuhara, *Sci. Technol. Adv. Mater.*, 2000, **1**, 219–225.